ARL13B-Cerulean rescues Arl13b-null mouse from embryonic lethality and reveals a role for ARL13B in spermatogenesis

Alyssa B. Long[1], Isabella M. Wilson[1,2], Tiffany T. Terry[1], Robert E. Van Sciver[1], and Tamara Caspary[1,□]

[1]Department of Human Genetics, Emory University School of Medicine, 615 Michael Street, Suite 301, Atlanta, GA 30322, USA
[2]Graduate Program in Molecular Biology, Emory University School of Medicine, 615 Michael Street, Suite 301, Atlanta, GA 30322, USA

[□]Address correspondence to: Tamara Caspary (tcaspar@emory.edu), 404-727-9862

ORCID and email for authors:
Alyssa B. Long 0000-0002-4467-4213, abushey@emory.edu
Isabella M. Wilson 0000-0002-6677-9622, Isabella.wilson@emory.edu
Tiffany T. Terry 0000-0002-2729-6281, tiffany.terry@emory.edu
Robert E. Van Sciver 0000-0002-1818-2661, rvansci@emory.edu
Tamara Caspary 0000-0002-6579-7589, tcaspar@emory.edu

Running title: Rescue of *Arl13b*-null lethality

Summary statement: Endogenous ARL13B, a regulatory GTPase enriched in cilia, can be functionally replaced by ARL13B-Cerulean expression in mouse development and is required for spermatogenesis.

ABSTRACT

ARL13B is a regulatory GTPase enriched in cilia, making it a popular marker for this organelle. *Arl13b*$^{hnn/hnn}$ mice lack ARL13B expression, die during midgestation, and exhibit defects in ciliogenesis. The *R26Arl13b-Fucci2aR* biosensor mouse line directs the expression of fluorescently tagged full-length *Arl13b* cDNA upon *Cre* recombination. To determine whether constitutive, ubiquitous expression of ARL13B-Cerulean can replace endogenous gene expression, we generated *Arl13b*$^{hnn/hnn}$ animals expressing ARL13B-Cerulean. We show that *Arl13b*$^{hnn/hnn}$*;Arl13b-Cerulean* mice survive to adulthood with no obvious physical or behavioral defects, indicating that the fluorescently tagged protein can functionally replace the endogenous protein during development. However, we observed that rescued males failed to sire offspring, revealing a role for ARL13B in spermatogenesis. This work shows that the *R26Arl13b-Fucci2aR* mouse contains an inducible allele of *Arl13b* capable of functioning in most tissues and biological processes.

KEY WORDS: ARL13B, cilia, lethality, infertility, spermatogenesis, inducible

INTRODUCTION

ARL13B is a regulatory GTPase that is enriched in cilia and is required for proper ciliogenesis and trafficking of signaling molecules (Caspary et al., 2007; Higginbotham et al., 2012; Larkins et al., 2011; Sun et al., 2004). Cilia are microtubule-based projections that can be non-motile or motile. Several transgenic models label cilia by fusing ARL13B to fluorescent proteins (Bangs et al., 2015; Borovina et al., 2010; Delling et al., 2013; Ford et al., 2018; Schmitz et al., 2017). These models display no obvious gain-of-function defects; embryos develop normally into viable adults and appear healthy overall. To date, analyses of these fluorescently labeled ARL13B models are solely in the context of ARL13B expressed from the endogenous locus.

Mice lacking ARL13B protein due to an ENU-induced mutation, *Arl13b*^{hnn}, die around embryonic day (E)13.5 and exhibit short cilia and defects in the structure of the ciliary axoneme (Caspary et al., 2007). *Arl13b*$^{hnn/hnn}$ embryos display abnormal Hedgehog (Hh) signaling, consistent with cilia being required to transduce Hh signaling in vertebrates (Caspary et al., 2007; Huangfu et al., 2003). Indeed, components of vertebrate Hh signaling are abnormally trafficked in *Arl13b*^{hnn} cilia (Larkins et al., 2011).

Conditional alleles of *Arl13b* circumvent embryonic lethality and show that ARL13B is critical for a variety of developmental processes. In the kidney, deletion of *Arl13b* leads to cystic kidneys (Augière et al., 2024; Bay et al., 2018; Duldulao et al., 2009; Li et al., 2016; Seixas et al., 2016; Sun et al., 2004). *Arl13b* deletion throughout the central nervous system leads to hydrocephaly (Su et al., 2012; Suciu et al., 2021). *Arl13b* deletion in specific subsets of neurons or interneurons reveals brain defects including small cerebellar vermis, impaired interneuron migration, and abnormal radial glial scaffolding (Guo et al., 2017; Higginbotham et al., 2012; Higginbotham et al., 2013; Suciu et al., 2021). ARL13B also functions in the specialized sensory cilia of the visual and olfactory systems (Dilan et al., 2019; Fiore et al., 2020; Habif et al., 2023; Hanke-Gogokhia et al., 2017; Joiner et al., 2015). Patients with the ciliopathy Joubert syndrome (JS) exhibit similar phenotypes, consistent with *ARL13B* mutations causing JS (OMIM 612291) (Cantagrel et al., 2008; Thomas et al., 2015).

Arl13b$^{V358A/V358A}$ mice are viable and fertile despite lacking ARL13B protein specifically in cilia. This engineered variant, ARL13B^{V358A}, retains the known

biochemical activities of ARL13B but is not detectable in cilia (Gigante et al., 2020; Higginbotham et al., 2012; Mariani et al., 2016). *Arl13b*$^{V358A/V358A}$ mice display enlarged, cystic kidneys, develop hyperphagia, and become obese, indicating ciliary ARL13B functions to regulate kidney development as well as energy homeostasis (Terry et al., 2023; Van Sciver et al., 2023). Hh signaling is normal in *Arl13b*$^{V358A/V358A}$ mice while ciliogenesis is abnormal, showing the two processes can be uncoupled and ciliary ARL13B regulates ciliogenesis (Gigante et al., 2020).

ARL13B's function in ciliogenesis varies by cell type. *Arl13b* loss in tissues including the left-right organizer, neural tube, and mesenchyme leads to short cilia, albeit at normal frequencies (Caspary et al., 2007; Duldulao et al., 2009; Larkins et al., 2011; Su et al., 2012). In contrast, cultured fibroblast cells derived from *Arl13b*$^{hnn/hnn}$ embryos exhibit short cilia at lower frequencies, and the efferent ducts of the mammalian male reproductive system display short motile cilia in normal numbers when *Arl13b* is deleted (Augière et al., 2024; Larkins et al., 2011). In the kidney, *Arl13b* deletion results in a complete absence of cilia (Duldulao et al., 2009; Li et al., 2016; Seixas et al., 2016; Sun et al., 2004). The mechanism(s) through which ARL13B controls ciliogenesis in any cell type remains unclear.

ARL13B expression levels correlate with cilia length in several cell types. While ARL13B loss leads to short or absent cilia, ARL13B overexpression can cause ciliary elongation (Larkins et al., 2011; Lu et al., 2015; Pintado et al., 2017). For example, primary wild-type or *Arl13b*$^{hnn/hnn}$ fibroblasts overexpressing *Arl13b* display longer cilia than untransfected cells (Larkins et al., 2011). Ciliary lengthening reflects tissue-specific functions of ARL13B in ciliogenesis. In the *R26Arl13b-Fucci2aR* biosensor mouse line, the expression of full-length, fluorescently tagged ARL13B-Cerulean results in longer cilia in cultured cells, the mesenchyme, kidney tubules, and liver bile ducts (Ford et al., 2018). Meanwhile, cilia of the nasal epithelium and brain ependyma remain the same length as in control mice (Ford et al., 2018). This suggests ARL13B-Cerulean is functional and differentially impacts ciliogenesis in distinct cell types.

The *R26Arl13b-Fucci2aR* biosensor carries a floxed-STOP cassette between the CAG promoter and the full-length *Arl13b* cDNA fused to Cerulean, providing spatial and temporal control of expression (Ford et al., 2018). It also constitutively expresses

mVenus and mCherry fused to fragments of hGem and hCdt1, enabling simultaneous monitoring of cilia and cell cycle progression (Ford et al., 2018; Sakaue-Sawano et al., 2008). The inclusion of full length *Arl13b* cDNA suggests functional protein is produced and implies the *R26Arl13b-Fucci2aR* biosensor might also serve as an inducible *Arl13b* allele. To test this, we asked whether the recombined allele expressing ubiquitous, constitutive ARL13B-Cerulean protein could replace endogenous ARL13B in the *Arl13b*$^{hnn/hnn}$ null mouse model. We also investigated the localization and level of ARL13B-Cerulean expression in several tissues where ARL13B functions.

RESULTS

Systemic expression of ARL13B-Cerulean rescues embryonic lethality of *Arl13b*$^{hnn/hnn}$ null mice

To generate *Arl13b*$^{hnn/hnn}$*;Arl13b-Cerulean* mice, we first crossed *R26Arl13b-Fucci2aR* mice with animals carrying *CMV-Cre* to indelibly activate biosensor expression in all tissues. For simplicity, we call this constitutively-on allele *Arl13b-Cerulean.* We bred *Arl13b-Cerulean* mice to animals carrying *Arl13b*^{hnn}, the *Arl13b*-null allele and intercrossed the *Arl13b*$^{hnn/+}$*;Arl13b-Cerulean* progeny. We determined the survival rate of pups two weeks after birth and performed genotyping. As expected, *Arl13b*$^{hnn/+}$*;Arl13b-Cerulean* intercrosses generated no viable *Arl13b*$^{hnn/hnn}$ mice, which are embryonic lethal (Fig. 1A). In contrast, we observed *Arl13b*$^{hnn/hnn}$*;Arl13b-Cerulean* mice at close to the predicted frequencies (Fig. 1A). The rescued *Arl13b*$^{hnn/hnn}$*;Arl13b-Cerulean* mice survived into adulthood and displayed no gross morphological or behavioral defects (Fig. 1B). Thus, we conclude that ARL13B-Cerulean functionally compensates for the loss of endogenous ARL13B protein during embryonic development, indicating it is an inducible allele.

As ciliary ARL13B regulates body weight, we investigated growth in *Arl13b*$^{hnn/hnn}$*;Arl13b-Cerulean* mice. We maintained cohorts of mice on breeder chow and measured body weight weekly from weaning (week three) to week twelve. We found no significant difference in weight curves between control (*Arl13b*$^{+/+}$ or *Arl13b*$^{hnn/+}$ with or without ARL13B-Cerulean) and *Arl13b*$^{hnn/hnn}$*;Arl13b-Cerulean* male or female

mice (Fig. 1C). *Arl13b*$^{hnn/hnn}$*;Arl13b-Cerulean* mice maintained normal body weight throughout adulthood (Fig. S1A,B). These data indicate that ARL13B-Cerulean functions to regulate body weight homeostasis.

To evaluate the relative expression levels of ARL13B and ARL13B-Cerulean protein, we performed western blots using lysates from E12.5 embryos. We observed endogenous ARL13B at approximately 60 kDa in all embryos except the *Arl13b*$^{hnn/hnn}$ mutants (Fig. 1D). We detected exogenous ARL13B-Cerulean fusion protein at approximately 72 kDa only in embryos carrying the biosensor (Fig. 1D). Lysates from embryos with two copies of the biosensor exhibited more ARL13B-Cerulean protein than those carrying one copy, although cleavage of the fusion protein complicated exact quantification (Fig. 1D, S1C). The stronger signal produced by ARL13B-Cerulean compared to endogenous ARL13B likely reflected a high level of *Arl13b-Cerulean* expression driven by the CAG promoter, but we cannot rule out a higher affinity of the antibody to the fusion protein. Taken together, these results show that ARL13B-Cerulean is robustly expressed and rescues the embryonic lethality in *Arl13b*$^{hnn/hnn}$ animals.

ARL13B-Cerulean expression restores wild-type levels of ciliation and cilia length to *Arl13b*$^{hnn/hnn}$ MEFs

To examine the ciliary localization of ARL13B and ARL13B-Cerulean in the *Arl13b*$^{hnn/hnn}$*;Arl13b-Cerulean* mice, we isolated and immortalized mouse embryonic fibroblasts (MEFs) from wild-type, *Arl13b*$^{hnn/hnn}$ and *Arl13b*$^{hnn/hnn}$*;Arl13b-Cerulean* E12.5 embryos. We co-stained cilia with antibodies against glutamylated tubulin (GT335) and ARL13B. We detected both glutamylated tubulin and ARL13B in wild-type *Arl13b*$^{+/+}$ cilia (Fig. 2A). Mutant *Arl13b*$^{hnn/hnn}$ cells lacked ciliary ARL13B protein and displayed short cilia (Fig. 2B,E). We saw ARL13B-Cerulean localizing to cilia in *Arl13b*$^{hnn/hnn}$*;Arl13b-Cerulean* cells using antibodies against either GFP, which recognizes the Cerulean tag, or ARL13B (Fig. 2C, S2A,B). These results show that ARL13B-Cerulean displays normal ciliary localization, consistent with the findings reported in *R26Arl13b-Fucci2a*$^{Tg/Tg}$ MEFs (Ford et al., 2018).

To test whether ARL13B-Cerulean rescued the ciliogenesis defects in *Arl13b*$^{hnn/hnn}$, we quantified the ciliation rate and cilia length in the MEF lines. We observed a 32% decrease in the frequency of ciliated cells (from 62.3 to 30.5%) and a 41% decrease in average cilia length (from 1.72 to 1.02 microns) in the *Arl13b*$^{hnn/hnn}$ MEFs compared to wild type (Fig. 2D,E). In contrast, we found 58% of *Arl13b*$^{hnn/hnn}$*;Arl13b-Cerulean* cells were ciliated, with a mean cilia length of 1.54 microns, similar to wild-type MEFs (Fig. 2D,E). We observed trends consistent with *Arl13b-Cerulean* zygosity modestly impacting ciliation and ciliary length but nothing reached significance, regardless of the *Arl13b* genotype (Fig. 2D,E). These data indicate that ARL13B-Cerulean rescues ciliation frequency and cilia length in *Arl13b*$^{hnn/hnn}$ MEFs.

To determine the relative ARL13B and ARL13B-Cerulean protein expression levels in the immortalized MEFs, we performed western blots on whole cell lysates. We detected ARL13B-Cerulean only in cell lines that carried the biosensor (Fig. S2C). In contrast to our findings in embryo lysates, we observed up to a 3-fold increase in ARL13B-Cerulean expression over ARL13B in the MEFs (Fig. S2D). We saw increased expression of ARL13B-Cerulean in wild-type MEFs with two copies of the biosensor compared to one, however precise quantification was again complicated by cleavage of the fusion protein (Fig. S2D).

To examine the relative transcript levels of *Arl13b* and *Arl13b-Cerulean*, we performed qRT-PCR using primers that differentiate between the 3' ends of the transcripts (Fig. S2E). We detected *Arl13b-Cerulean* only in samples carrying the biosensor (Fig. S2F). In addition, we observed more *Arl13b-Cerulean* transcript in *Arl13b*$^{+/+}$ or *Arl13b*$^{hnn/hnn}$ samples with 2 copies of the biosensor compared to those with 1 copy (Fig. S2F). Despite these trends, increased amounts of mRNA or protein do not correlate with any change in ciliation rate or cilia length in the immortalized MEFs (Fig. 2D,E). Taken together, these data indicate that *Arl13b-Cerulean* rescues the *Arl13b*$^{hnn/hnn}$ cilia phenotypes, and the zygosity of the biosensor does not impact the rescue.

Arl13b$^{hnn/hnn}$;Arl13b-Cerulean kidneys do not develop cysts

As ciliary ARL13B regulates kidney development, we examined *Arl13b$^{hnn/hnn}$;Arl13b-Cerulean* kidneys. We performed histology to assess tissue structure and immunofluorescence staining to monitor cilia. We saw normal kidney architecture and ARL13B-positive cilia in *Arl13b$^{+/+}$* and *Arl13b$^{hnn/+}$;Arl13b-Cerulean* mice (Fig. 3A,B). In contrast to *Arl13b$^{V358A/V358A}$* mice that express cilia-excluded ARL13B^{V358A} and develop kidney cysts by four weeks of age, adult *Arl13b$^{hnn/hnn}$;Arl13b-Cerulean* mice did not have cystic kidneys (Fig. 3C) (Van Sciver et al., 2023). Of note, we found increased intra- and inter-tubule dilations in *Arl13b$^{hnn/hnn}$;Arl13b-Cerulean* kidneys, which may be due to interstitial edema, fibrosis, or inflammation (Fig. 3C). To investigate whether fibrosis was contributing to this phenotype, we performed Sirius Red staining on kidney sections. We found no appreciable fibrosis in *Arl13b$^{hnn/hnn}$;Arl13b-Cerulean* kidneys, indicating fibrosis did not underlie the dilations (Fig. S3A-C). We observed ARL13B-positive cilia in kidney tubules of all three genotypes (Fig. 3A-C). In male *Arl13b$^{hnn/hnn}$;Arl13b-Cerulean* mice, we observed a slight increase in total kidney weight to body weight ratio; there was no difference in females (Fig. 3D). We saw no change in gross morphology of the *Arl13b$^{hnn/hnn}$;Arl13b-Cerulean* kidneys of either sex compared to controls (Fig. 3E). *Arl13b$^{hnn/hnn}$;Arl13b-Cerulean* mice exhibited kidney weight to body weight ratios comparable to controls through 24 weeks, indicating they did not develop cystic kidneys later in life (Fig. S3D,E). Altogether these results indicate ARL13B-Cerulean is sufficient to support normal kidney ciliation and morphology.

Cerebellar patterning is normal in *Arl13b$^{hnn/hnn}$;Arl13b-Cerulean* mice

To determine whether ARL13B-Cerulean is functional in the brain, we examined *Arl13b$^{hnn/hnn}$;Arl13b-Cerulean* brain morphology, focusing on the cerebellum. We performed hematoxylin-eosin staining on cerebellar sections, and found patterning and size were comparable between control (*Arl13b$^{hnn/+}$*) and *Arl13b$^{hnn/hnn}$;Arl13b-Cerulean* mice (Fig. 4A). ARL13B-positive cilia were present at the Purkinje cell layer (PCL) interface between the outer molecular layer (ML) and the inner granule layer (IGL) in *Arl13b$^{+/+}$*, *Arl13b$^{hnn/+}$;Arl13b-Cerulean* and *Arl13b$^{hnn/hnn}$;Arl13b-Cerulean* cerebella (Fig. 4B). Choroid plexus cilia in *Arl13b$^{hnn/hnn}$;Arl13b-Cerulean* brains were visible with

antibodies against ARL13B or GFP (Fig. 4C). We saw no overt hydrocephaly in *Arl13b*$^{hnn/hnn}$*;Arl13b-Cerulean* mice, although we noted slight enlargement of the lateral ventricle lumens compared to control animals (Fig. S4A). To determine the ARL13B and ARL13B-Cerulean protein levels in cerebella, we performed immunoblot on lysates from adult tissues. We detected roughly twice the level of ARL13B-Cerulean compared to endogenous ARL13B protein in cerebella that carried the biosensor (Fig. S4B-D). These findings demonstrate that brain development is grossly normal in *Arl13b*$^{hnn/hnn}$*;Arl13b-Cerulean* animals.

Pancreatic islet cilia are easily identified in *Arl13b*$^{hnn/hnn}$*;Arl13b-Cerulean* mice

We examined the pancreas, a ciliated organ where ARL13B is clearly expressed (Cho et al., 2022; Li et al., 2021; Li et al., 2022). We evaluated *Arl13b*$^{hnn/hnn}$*;Arl13b-Cerulean* tissue morphology in sections stained with hematoxylin-eosin. We saw an increase in interstitial space surrounding the acinar cells of the *Arl13b*$^{hnn/hnn}$*;Arl13b-Cerulean* pancreas compared to the control (Fig. 5A). We performed immunofluorescent staining and detected glucagon-producing alpha and insulin-producing beta cells normally arranged in islets of *Arl13b*$^{hnn/hnn}$*;Arl13b-Cerulean* mice (Fig. 5B). We also observed ARL13B-positive cilia in islets from each of the groups, with overlapping GFP-positive staining in mice expressing ARL13B-Cerulean (Fig. 5C). These data indicate the pancreas develops normally in *Arl13b*$^{hnn/hnn}$*;Arl13b-Cerulean* mice.

***Arl13b*$^{hnn/hnn}$*;Arl13b-Cerulean* males are infertile due to absence of mature sperm**

In the course of phenotyping, we mated *Arl13b*$^{hnn/hnn}$*;Arl13b-Cerulean* with control *Arl13b*$^{hnn/+}$*;Arl13b-Cerulean* mice. Females of either genotype or male control *Arl13b*$^{hnn/+}$*;Arl13b-Cerulean* mice produced litters of normal size (Fig. 6A,B). In contrast, *Arl13b*$^{hnn/hnn}$*;Arl13b-Cerulean* males did not produce any litters during 6-8 weeks of mating even though we detected copulation plugs, indicating mating behavior is normal (Fig. 6B). We examined testis weight to body weight ratios and found no significant differences between *Arl13b*$^{hnn/hnn}$*;Arl13b-Cerulean* and control mice (Fig. 6C, S5A).

To investigate the *Arl13b*$^{hnn/hnn}$*;Arl13b-Cerulean* male infertility, we analyzed testis sections stained with periodic acid-Schiff reagent and hematoxylin (PAS-H). The

Arl13b$^{hnn/hnn}$*;Arl13b-Cerulean* seminiferous tubule architecture was largely normal (Fig. 6D). The presence and patterning of germline (spermatogonia, spermatocytes) and support cells (Sertoli, Leydig) in *Arl13b*$^{hnn/hnn}$*;Arl13b-Cerulean* testes did not differ from wild type (Fig. 6D). We identified both round and elongating spermatids in the *Arl13b*$^{hnn/hnn}$*;Arl13b-Cerulean* testis, consistent with normal meiosis (Fig. 6D). In later stages of spermatogenesis, elongating spermatids migrated toward the tubule lumen and sperm flagella were visible in the control testis (Fig. 6D). We had difficulty detecting mature sperm at the luminal surface of *Arl13b*$^{hnn/hnn}$*;Arl13b-Cerulean* seminiferous tubules and did not observe sperm flagella in the lumen by histology (Fig. 6D). In addition, we could not visualize normal sperm in the *Arl13b*$^{hnn/hnn}$*;Arl13b-Cerulean* cauda epididymis (Fig. 6E). Instead, the epididymides of *Arl13b*$^{hnn/hnn}$*;Arl13b-Cerulean* mice appeared empty or contained cellular debris (Fig. 6E). These data indicate the *Arl13b*$^{hnn/hnn}$*;Arl13b-Cerulean* testis lacks mature flagellated sperm.

Nuclear condensation, acrosome formation, and flagellum biosynthesis occur during the final phase of spermatogenesis. We looked at nuclei (stained with Hoechst), centrosomes (stained with antibody against fibroblast growth factor receptor 1 oncogene partner, FGFR1OP, aka FOP), the acrosome (marked with peanut agglutinin, PNA), and flagella (stained with antibodies against acetylated tubulin) in testis sections from wild-type and *Arl13b*$^{hnn/hnn}$*;Arl13b-Cerulean* mice. We observed defects in the nucleus, acrosome, and flagellum morphology of *Arl13b*$^{hnn/hnn}$*;Arl13b-Cerulean* sperm, suggesting defects in multiple aspects of sperm maturation (Fig. 6F).

To examine spermatid head and tail morphology, we isolated sperm from wild-type, *Arl13b*$^{hnn/+}$*;Arl13b-Cerulean* and *Arl13b*$^{hnn/hnn}$*;Arl13b-Cerulean* males and stained with Hoechst, PNA, and acetylated tubulin. Overall, wild-type and control sperm displayed falciform heads with condensed nuclei and normal acrosomes as well as long flagella, whereas *Arl13b*$^{hnn/hnn}$*;Arl13b-Cerulean* sperm exhibited abnormal heads and short, misshapen flagella (Fig. 6G). As we observed in the testis sections, the *Arl13b*$^{hnn/hnn}$*;Arl13b-Cerulean* sperm displayed defects in acrosome formation and nuclear condensation (Fig. 6G). In addition, *Arl13b*$^{hnn/hnn}$*;Arl13b-Cerulean* sperm tails were shorter than controls, with a mean length of 19.2 compared to 110.6 microns (Fig. 6G**,** S5B).

To determine the impact of this flagellar defect on sperm motility, we analyzed sperm characteristics using computer-assisted sperm analysis (CASA) software. This revealed *Arl13b*$^{hnn/hnn}$*;Arl13b-Cerulean* sperm were present at low concentration (5.17 vs 84.24 million per ml) and exhibited poor motility (0.19 vs 26.61 million per ml) compared to wild type (Fig. S5C-E). The combined sperm characteristics of low count, poor motility, and abnormal morphology are termed oligoasthenoteratozoospermia (OAT), a common clinical presentation of male infertility. Collectively, our results show that ARL13B-Cerulean is unable to compensate for endogenous ARL13B function in the male reproductive system, resulting in OAT in mice.

One possible explanation for the infertility and sperm morphology phenotype is that ARL13B-Cerulean expression interferes with normal ARL13B function despite not causing phenotypes in other tissues. However, we observed no reproductive or phenotypic differences in *Arl13b*$^{+/+}$ or *Arl13b*$^{hnn/+}$ males carrying one or two copies of *Arl13b-Cerulean* compared to those lacking the biosensor, arguing against ARL13B-Cerulean expression possessing a gain-of-function effect (Fig. 6).

Taken together, our results showed that ARL13B plays a critical role in sperm maturation and development. Furthermore, the infertility phenotype suggests that ARL13B-Cerulean expression differs from that of endogenous ARL13B in a manner that renders ARL13B-Cerulean unable to compensate for endogenous ARL13B function in the male reproductive system.

ARL13B-Cerulean is expressed in the testis and sperm

We investigated the expression levels of ARL13B and ARL13B-Cerulean in testis via western blot. We observed both proteins were present and that ARL13B is expressed at low levels (Fig. 7A, S6A,B). Indeed, endogenous ARL13B appears to be expressed at lower levels than in other tissues we examined (compare Fig. 7A to 1D, S2C, S4B).

To determine where ARL13B and ARL13B-Cerulean are expressed *in situ*, we performed immunofluorescent staining on wild-type and *Arl13b*$^{hnn/hnn}$*;Arl13b-Cerulean* testis sections. We detected a few ARL13B-positive cilia on cells located near the basal membrane of *Arl13b*$^{+/+}$ seminiferous tubules (Fig. 7B). In *Arl13b*$^{hnn/hnn}$*;Arl13b-Cerulean*

testis, we also identified these cilia with GFP antibody, indicating that both endogenous ARL13B and ARL13B-Cerulean were expressed in these support cells (Fig. 7B). The basal and myoid cells of *Arl13b*$^{+/+}$ and *Arl13b*$^{hnn/hnn}$*;Arl13b-Cerulean* epididymides exhibited similar infrequent cilia (Fig. S6C).

To investigate the intracellular location of the ARL13B and ARL13B-Cerulean proteins, we stained isolated sperm with antibodies against ARL13B and GFP. We were unable to detect ARL13B in wild-type sperm by immunostaining, saw faint expression in the head and midpiece of *Arl13b*$^{hnn/+}$*;Arl13b-Cerulean* sperm, and observed higher levels of expression along the whole length of *Arl13b*$^{hnn/hnn}$*;Arl13b-Cerulean* sperm (Fig. 7C). These data are consistent with the levels of protein expression we detected in testis by western blot. We saw increased fluorescence of ARL13B-Cerulean from control *Arl13b*$^{hnn/+}$*;Arl13b-Cerulean* to *Arl13b*$^{hnn/hnn}$*;Arl13b-Cerulean* when we stained with anti-GFP antibodies (Fig. 7C). Taken together, our data indicate that the ARL13B-Cerulean biosensor is functional in most tissues during development and reveals an essential role for ARL13B in spermiogenesis.

DISCUSSION

Here, we showed that the ARL13B-Cerulean protein expressed by the *R26Arl13b-Fucci2aR* biosensor compensates for the loss of endogenous ARL13B in *Arl13b*$^{hnn/hnn}$ mice. We found that *Arl13b*$^{hnn/hnn}$*;Arl13b-Cerulean* mice developed normally and survived into adulthood without gross morphological or behavioral defects indicating *R26Arl13b-Fucci2aR* is an inducible, functional *Arl13b* allele. Rescuing the embryonic lethality of *Arl13b*$^{hnn/hnn}$ allowed us to examine the function of ARL13B-Cerulean in several organs. We observed normal tissue anatomy and ciliation in the *Arl13b*$^{hnn/hnn}$*;Arl13b-Cerulean* kidney, brain, and pancreas. In addition, we examined the localization and expression level of ARL13B-Cerulean in these organs and detected normal ciliary enrichment and robust protein expression. Surprisingly, *Arl13b*$^{hnn/hnn}$*;Arl13b-Cerulean* males were infertile. They exhibited low sperm counts, low sperm motility, and abnormal sperm shape – with short flagella and atypical acrosome structures. These findings suggest that ARL13B-Cerulean can functionally replace

ARL13B in most developmental processes and reveal that endogenous ARL13B is required for normal spermatogenesis.

One unanticipated result of this work was that expression of ARL13B-Cerulean did not result in overt cilia phenotypes. We observed higher levels of ARL13B-Cerulean than ARL13B protein in embryo, MEF, cerebellum, and testis lysates, but did not see significant increases in ciliary length. This contrasts with previous findings *in vivo* where *Arl13b* gene dosage directly correlates with ciliary length. Cilia are longer upon *Arl13b* overexpression in zebrafish or *Arl13b-mCherry* transgene expression in mice (Bangs et al., 2015; Lu et al., 2015; Pintado et al., 2017). Similarly, wild-type primary MEFs carrying two copies of the *Arl13b-Cerulean* biosensor display longer cilia (Ford et al., 2018). In wild-type mice homozygous for *Arl13b-Cerulean*, cilia are longer in several tissues, although other tissues did not show this change (Ford et al., 2018). One possibility is that cilia lengthening results from high levels of ARL13B. Perhaps the immortalization of MEFs in our study selected for ARL13B protein levels that don't reach this threshold. Furthermore, *in vivo Arl13b* overexpression has proven challenging: the broadly used *Arl13b-mCherry* transgenic mouse is the only line (of four founders) that has consistent expression and the *Arl13b-EGFP* transgenic mouse is one of only two founders (Bangs et al., 2015; Delling et al., 2013). As transgenesis typically produces many more founders, the few ARL13B-expressing founders may reflect the fact that high ARL13B levels are not compatible with life. Thus, the protein levels of ARL13B-Cerulean may undergo similar selective pressure. In any case, ARL13B-Cerulean can functionally replace endogenous ARL13B with no adverse effects on growth and development.

This work reveals a novel function for ARL13B in spermatogenesis. ARL13B localizes to primary cilia of basal cells in the adult mouse epididymis and functions in the male reproductive system to affect fluid flow and immune response (Augière et al., 2024; Bernet et al., 2018; Girardet et al., 2020; Girardet et al., 2022). However, ARL13B is not known to function in the germline. We predicted that the spermatogenesis defect is due to abnormal ARL13B-Cerulean expression in the testis. Although endogenous ARL13B protein levels are lower in testis than in cerebellum or embryo lysates, we found that ARL13B-Cerulean is robustly expressed in the *Arl13b*$^{hnn/hnn}$*;Arl13b-Cerulean*

testis as well as in isolated sperm. Mice lacking ARL13B specifically in cilia, *Arl13b*$^{V358A/V358A}$, are viable and fertile so one possibility is that cellular ARL13B plays a critical function in spermatogenesis (Gigante et al., 2020). Answering this question will likely require using the *Arl13b*^{flox} conditional null allele and appropriate Cre lines, which will also address issues of cell autonomy.

The cause of the defective spermatogenesis we observed in *Arl13b*$^{hnn/hnn}$*;Arl13b-Cerulean* is unclear. It is unlikely that the biosensor had a gain-of-function or dominant-negative phenotype as *Arl13b*$^{+/+}$ and *Arl13b*$^{hnn/+}$ males carrying *Arl13b-Cerulean* were fertile. Notably, the full-length *Arl13b* cDNA fused to Cerulean differs from endogenous ARL13B mRNA. Distinct isoforms of proteins are expressed exclusively in somatic or germ cells (Eisa et al., 2021; Grassi et al., 2022; Konno et al., 2015; Nielsen and Raff, 2002). Perhaps specific ARL13B isoforms are expressed in the germline. Alternatively, the role of ARL13B in building a flagellum during spermatogenesis could be specific to flagellogenesis. While flagella and cilia possess axonemes, they also contain different components and perform distinct functions. For instance, mammalian sperm flagella have unique accessory structures such as the mitochondrial sheath, outer dense fibers, and the fibrous sheath. ARL13B may normally interact with specific partners to contribute to the building of the flagellum, and ARL13B-Cerulean may be unable to replace endogenous protein for those interactions. Clearly, some difference between endogenous ARL13B and ARL13B-Cerulean is functionally relevant to spermatogenesis.

A key feature of the regulatory GTPase family to which ARL13B belongs is the ability to work with distinct effector proteins depending on cell type, subcellular location, or timing. It is possible that ARL13B has effectors specific to the testis or germline that play a role during spermatogenesis (nuclear condensation, acrosome formation, flagella outgrowth). On the other hand, some of ARL13B's known effectors regulate spermatogenesis, suggesting the defects reflect a more general function of ARL13B. For example, ARL13B associates with the exocyst complex to regulate intracellular vesicle trafficking, with the BBSome to facilitate cargo coupling on the membrane, and with members of the IFT-B complex to regulate ciliary traffic (Barral et al., 2012; Cevik et al., 2013; Liu et al., 2023; Nozaki et al., 2017). Conditional deletion of *Exoc1*, encoding

an exocyst component, in spermatogonia leads to spermatocyte aggregation and impaired fertility (Osawa et al., 2021). Mice carrying mutations in BBSome subunits exhibit male infertility due to an absence of sperm flagella (Davis et al., 2007; Mykytyn et al., 2004; Nishimura et al., 2004). Similarly, mutations in IFT proteins result in defective sperm morphology, quantity, and/or motility (Liu et al., 2017; San Agustin et al., 2015; Shi et al., 2019; Zhang et al., 2016; Zhang et al., 2017). Further work is needed to determine whether these effectors contribute to the mechanism(s) underlying the infertility we observed in the *Arl13b*$^{hnn/hnn}$*;Arl13b-Cerulean* males.

In summary, our data show that full-length *Arl13b* cDNA with a Cerulean tag can functionally replace the endogenous *Arl13b* gene in several tissues and biological processes, with the notable exception of spermatogenesis. Future studies are required to determine the cell types that require ARL13B for spermatogenesis as well as the mechanism by which ARL13B regulates spermatogenesis. Our findings expand upon previous work illustrating that the *R26Arl13b-Fucci2aR* biosensor is a powerful tool to monitor cilia and cell cycle progression. Our work is significant in demonstrating that *Arl13b-Cerulean* is a functional, inducible allele of *Arl13b*.

MATERIALS AND METHODS

Mice

All animal experiments were approved by the Institutional Animal Care and Use Committee of Emory University and were performed in compliance with guidelines established by the National Institute of Health. Mouse alleles used in this study were *Arl13b*^{hnn} (MGI:3578151), *CMV-cre* (Tg(CMV-cre)1Cgn, MGI:2176180) acquired from the Jackson Laboratory (RRID:IMSR_JAX:006054), and *R26Arl13b-Fucci2aR* (Gt(ROSA)26Sor$^{tm1(CAG-Cerulean/Arl13b,-Venus/GMNN,-Cherry/CDT1)Rmort}$, MGI:6193734) purchased from EMMA (EM:12168). Adult animals were over 8 weeks of age. Genotyping was performed on biopsied samples (ear punch or yolk sac) by Transnetyx using real-time PCR.

Antibodies and reagents

Antibodies used in this study are listed in Table S1.

Cell culture

MEFs were derived from E12.5 mouse embryos and cultured in DMEM supplemented with 10% fetal bovine serum (FBS) and 1% penicillin/streptomycin at 5% CO_2 at 37°C. MEFs were immortalized by transfection with a plasmid containing the large T antigen of SV40.

For immunofluorescence, immortalized MEFs were plated on glass coverslips and serum-starved for 24 hours in DMEM supplemented with 0.5% FBS. Cells were fixed in 4% paraformaldehyde (PFA) for 10 minutes, washed 3x with phosphate-buffered saline (PBS) for 5 minutes each, and blocked with tris buffered saline (TBS) + 5% goat serum + 0.1% Triton X-100 (blocking buffer) for 10 minutes. Cells were incubated with primary antibodies diluted in blocking buffer overnight at 4°C, washed 3x with blocking buffer for 5 minutes each, and incubated with secondary antibodies diluted in blocking buffer for 1 hour at room temperature in the dark. Finally, cells were washed 3x with blocking buffer for 5 minutes each and mounted onto glass slides using Prolong Gold.

Images were obtained with a BioTek Lionheart FX automated microscope (Agilent) and processed with Gen5 imaging software (version 3.11, Agilent) and FIJI (release 2.16.0) (Schindelin et al., 2012). For cilia counts, we quantified the number of nuclei and glutamylated tubulin-positive cilia in each field of view with multiple fields imaged. To determine cilia length, the CiliaQ plugin for FIJI was used with measurements taken using the glutamylated tubulin channel (Hansen et al., 2021).

Western blot

Lysates were obtained by homogenizing tissue with Pierce RIPA Buffer (ThermoScientific) containing protease inhibitor cocktail (Sigma Aldrich) using a mechanical pestle. After sonication on ice, lysates were incubated at 4°C for 30 minutes turning end-over-end. Lysates were centrifuged at 13000 rpm for 15 minutes at 4°C and the protein content of the supernatant was determined using the Pierce BCA Protein

Assay (ThermoScientific). Equal amounts (30µg) of protein were separated by SDS-PAGE and transferred onto nitrocellulose membranes. After blocking with StartingBlock T20 PBS (ThermoScientific) (antibody block) for at least 1 hour, membranes were incubated with primary antibodies diluted in antibody block for 1 hour at room temperature or overnight at 4°C. Primary antibodies were detected using fluorescently-conjugated secondary antibodies. The Azure600 imaging system (Azure Biosystems) and FIJI software were used to visualize and quantify proteins, with anti-actin-rhodamine loading control used to normalize band intensity.

Histological analyses

Mice were perfused transcardially with 4% PFA in PBS. Organs were dissected, postfixed in 4% PFA (kidney, pancreas, brain) or Bouin's fixative (testis) overnight at 4°C, then dehydrated in ethanol for paraffin embedding or cryoprotected with 30% sucrose in phosphate buffer then embedded in Tissue-Tek OCT compound (Sakura) for frozen sectioning. Paraffin sections (kidney, testis, pancreas) were acquired at 5 µm and frozen sections (brain) were acquired at 10 µm. Sections were mounted onto Superfrost Plus microscope slides.

For histology, deparaffinized or rehydrated frozen sections were stained with hematoxylin and eosin, Sirius Red and fast green, or periodic acid and Schiff's reagent with hematoxylin (PAS-H) following standard protocols. Slides were coverslipped with Cytoseal 60 (Epredia). For immunofluorescence, antigen retrieval was performed on deparaffinized sections using hot 10 mM citrate buffer, pH 6.0, before incubation with primary antibodies overnight at 4°C. Sections were then incubated with fluorescent secondary antibodies and Hoechst, and coverslipped with Prolong Gold (ThermoFisher).

Quantitative reverse transcriptase PCR (qRT-PCR)

Cells were collected, snap frozen, and stored at -80°C. RLT lysis buffer (Qiagen) was added, and RNA was purified with the RNeasy Mini Kit (Qiagen) according to the manufacturer's protocol. Potential genomic DNA contamination was eliminated by incubation with RNase-free DNase (Qiagen). To generate cDNA, total RNA was reverse

transcribed using iScript (Bio-Rad). The SsoAdvanced Universal SYBR Green Supermix kit (Bio-Rad) was used to perform real-time PCR on prepared cDNA. Each reaction was performed in triplicate for each biological sample and normalized to *Gapdh*. Primers were: *FucciQ "F3"*: 5'-GTGATGCTCAGGACACGATC-3'; *FucciQ 'R3"*: 5'-CGGTGGTGCAGATGAACTTC-3'; *Arl13bQ "R4"*: 5'-TTGTCTTGCCCATCATCAGC-3'; *Gapdh-F*: 5'-CGTCCCGTAGACAAAATGGT-3'; *Gapdh-R*: 5'-GAATTTGCCGTGAGTGGAGT-3'.

Sperm isolation and staining

The epididymis was dissected and kept in a Petri dish containing PBS. Sperm were released from the cauda epididymis by puncturing the tissue with fine forceps. The sperm suspension was placed on a glass-bottom 35 mm dish and incubated for 30 minutes in a CO_2 incubator at 37°C. Next, the sperm cells were fixed in 4% PFA in PBS for 10 minutes at room temperature, permeabilized and blocked for 1 hour in TBS + 5% goat serum + 0.1% Triton X-100 (blocking buffer) and incubated with primary antibodies diluted in blocking buffer for 1 hour at room temperature. After washing 3x with blocking buffer for 5 minutes each, cells were incubated with secondary antibodies diluted in blocking buffer for 1 hour at room temperature in the dark. Another 3x washes with blocking buffer for 5 minutes each were followed by the addition of glass coverslips using Prolong Gold as the mounting medium.

Statistical analyses

Data were analyzed by chi-squared test, unpaired *t*-test, or one-way ANOVA as indicated using Prism version 10.4.1 (GraphPad). Summarized data are presented as the mean ± standard deviation. Images are representative of a minimum of three biological samples and sample numbers for summarized data are indicated on the graph.

Acknowledgments

We thank lab members R. Bear, and H. Truong for discussion and comments on the manuscript, Emory University's NextGen 2024 summer high school students for

piloting the histology staining procedures, and K. Nitsche from the Emory University Mouse Transgenic and Gene Targeting Core (RRID:SCR_023535) for conducting the CASA procedure.

The cryopreserved B6;129P2-Gt(ROSA)26Sor$^{tm1(CAG-Cerulean/Arl13b,-Venus/GMNN,-Cherry/CDT1)Rmort}$/H sperm was obtained from the Mary Lyon Centre at MRC Harwell which distributes this strain on behalf of the European Mouse Mutant Archive (EM:12168). These mice were originally produced at the University of Lancaster.

Competing interests

The authors declare no competing or financial interests.

Author contributions

Conceptualization: A.B.L., I.M.W., T.T.T., R.E.V.S., T.C.

Methodology: A.B.L., T.T.T., R.E.V.S.

Formal analysis: A.B.L., I.M.W., T.T.T.

Investigation: A.B.L., I.M.W., T.T.T.

Writing – original draft: A.B.L.

Writing – review & editing: A.B.L., I.M.W., T.T.T., R.E.V.S., T.C.

Visualization: A.B.L., T.T.T., R.E.V.S.

Supervision: T.C.

Project administration: T.C.

Funding acquisition: T.C.

Funding

This work was supported in part by grants from the National Institutes of Health (GM148416 and DK128902 to T.C., DK127848 to R.E.V.S., DK137409 to T.T.T.).

Data availability

All relevant data can be found within the article and its supplementary information.

REFERENCES

Augière, C., Campolina-Silva, G., Vijayakumaran, A., Medagedara, O., Lavoie-Ouellet, C., Joly Beauparlant, C., Droit, A., Barrachina, F., Ottino, K., Battistone, M. A., et al. (2024). ARL13B controls male reproductive tract physiology through primary and motile cilia. *Commun. Biol.* 7, 1318.

Bangs, F. K., Schrode, N., Hadjantonakis, A.-K. and Anderson, K. V. (2015). Lineage specificity of primary cilia in the mouse embryo. *Nat. Cell Biol.* 17, 113–122.

Barral, D. C., Garg, S., Casalou, C., Watts, G. F. M., Sandoval, J. L., Ramalho, J. S., Hsu, V. W. and Brenner, M. B. (2012). Arl13b regulates endocytic recycling traffic. *Proc. Natl. Acad. Sci.* 109, 21354–21359.

Bay, S. N., Long, A. B. and Caspary, T. (2018). Disruption of the ciliary GTPase Arl13b suppresses Sonic hedgehog overactivation and inhibits medulloblastoma formation. *Proc. Natl. Acad. Sci.* 115, 1570–1575.

Borovina, A., Superina, S., Voskas, D. and Ciruna, B. (2010). Vangl2 directs the posterior tilting and asymmetric localization of motile primary cilia. *Nat. Cell Biol.* 12, 407–412.

Cantagrel, V., Silhavy, J. L., Bielas, S. L., Swistun, D., Marsh, S. E., Bertrand, J. Y., Audollent, S., Attié-Bitach, T., Holden, K. R., Dobyns, W. B., et al. (2008). Mutations in the cilia gene ARL13B lead to the classical form of Joubert syndrome. *Am. J. Hum. Genet.* 83, 170–179.

Caspary, T., Larkins, C. E. and Anderson, K. V. (2007). The graded response to Sonic hedgehog depends on cilia architecture. *Dev. Cell* 12, 767–778.

Cevik, S., Sanders, A. A. W. M., Van Wijk, E., Boldt, K., Clarke, L., Van Reeuwijk, J., Hori, Y., Horn, N., Hetterschijt, L., Wdowicz, A., et al. (2013). Active transport and diffusion barriers restrict Joubert Syndrome-associated ARL13B/ARL-13 to an Inv-like ciliary membrane subdomain. *PLoS Genet.* 9, e1003977.

Cho, J. H., Li, Z. A., Zhu, L., Muegge, B. D., Roseman, H. F., Lee, E. Y., Utterback, T., Woodhams, L. G., Bayly, P. V. and Hughes, J. W. (2022). Islet primary cilia motility controls insulin secretion. *Sci. Adv.* 8, eabq8486.

Davis, R., Swiderski, R., Rahmouni, K., Nishimura, D., Mullins, R., Agassandian, K., Philp, A., Searby, C., Andrews, M., Thompson, S., et al. (2007). A knockin mouse

model of the Bardet–Biedl syndrome 1 M390R mutation has cilia defects, ventriculomegaly, retinopathy, and obesity. *Proc. Natl. Acad. Sci. U. S. A.* 104, 19422–19427.

Delling, M., DeCaen, P. G., Doerner, J. F., Febvay, S. and Clapham, D. E. (2013). Primary cilia are specialized calcium signalling organelles. *Nature* 504, 311–314.

Dilan, T. L., Moye, A. R., Salido, E. M., Saravanan, T., Kolandaivelu, S., Goldberg, A. F. X. and Ramamurthy, V. (2019). ARL13B, a Joubert Syndrome-associated protein, is critical for retinogenesis and elaboration of mouse photoreceptor outer segments. *J. Neurosci.* 39, 1347–1364.

Duldulao, N. A., Lee, S. and Sun, Z. (2009). Cilia localization is essential for in vivo functions of the Joubert syndrome protein Arl13b/Scorpion. *Development* 136, 4033–4042.

Eisa, A., Dey, S., Ignatious, A., Nofal, W., Hess, R. A., Kurokawa, M., Kline, D. and Vijayaraghavan, S. (2021). The protein YWHAE (14-3-3 epsilon) in spermatozoa is essential for male fertility. *Andrology* 9, 312–328.

Fiore, L., Takata, N., Acosta, S., Ma, W., Pandit, T., Oxendine, M. and Oliver, G. (2020). Optic vesicle morphogenesis requires primary cilia. *Dev. Biol.* 462, 119–128.

Ford, M. J., Yeyati, P. L., Mali, G. R., Keighren, M. A., Waddell, S. H., Mjoseng, H. K., Douglas, A. T., Hall, E. A., Sakaue-Sawano, A., Miyawaki, A., et al. (2018). A cell/cilia cycle biosensor for single-cell kinetics reveals persistence of cilia after G1/S transition is a general property in cells and mice. *Dev. Cell* 47, 509-523.e5.

Gigante, E. D., Taylor, M. R., Ivanova, A. A., Kahn, R. A. and Caspary, T. (2020). ARL13B regulates Sonic hedgehog signaling from outside primary cilia. *eLife* 9, e50434.

Grassi, S., Bisconti, M., Martinet, B., Arcolia, V., Simon, J.-F., Wattiez, R., Leroy, B. and Hennebert, E. (2022). Targeted analysis of HSP70 isoforms in human spermatozoa in the context of capacitation and motility. *Int. J. Mol. Sci.* 23, 6497.

Guo, J., Otis, J. M., Higginbotham, H., Monckton, C., Cheng, J., Asokan, A., Mykytyn, K., Caspary, T., Stuber, G. D. and Anton, E. S. (2017). Primary cilia signaling shapes the development of interneuronal connectivity. *Dev. Cell* 42, 286-300.e4.

Habif, J. C., Xie, C., De Celis, C., Ukhanov, K., Green, W. W., Moretta, J. C., Zhang, L., Campbell, R. J. and Martens, J. R. (2023). The role of a ciliary GTPase in the regulation of neuronal maturation of olfactory sensory neurons. *Development* 150, dev201116.

Hanke-Gogokhia, C., Wu, Z., Sharif, A., Yazigi, H., Frederick, J. M. and Baehr, W. (2017). The guanine nucleotide exchange factor Arf-like protein 13b is essential for assembly of the mouse photoreceptor transition zone and outer segment. *J. Biol. Chem.* 292, 21442–21456.

Hansen, J. N., Rassmann, S., Stüven, B., Jurisch-Yaksi, N. and Wachten, D. (2021). CiliaQ: a simple, open-source software for automated quantification of ciliary morphology and fluorescence in 2D, 3D, and 4D images. *Eur. Phys. J. E Soft Matter* 44, 18.

Higginbotham, H., Eom, T.-Y., Mariani, L. E., Bachleda, A., Hirt, J., Gukassyan, V., Cusack, C. L., Lai, C., Caspary, T. and Anton, E. S. (2012). Arl13b in primary cilia regulates the migration and placement of interneurons in the developing cerebral cortex. *Dev. Cell* 23, 925–938.

Higginbotham, H., Guo, J., Yokota, Y., Umberger, N. L., Su, C.-Y., Li, J., Verma, N., Hirt, J., Ghukasyan, V., Caspary, T., et al. (2013). Arl13b-regulated cilia activities are essential for polarized radial glial scaffold formation. *Nat. Neurosci.* 16, 1000–1007.

Huangfu, D., Liu, A., Rakeman, A. S., Murcia, N. S., Niswander, L. and Anderson, K. V. (2003). Hedgehog signalling in the mouse requires intraflagellar transport proteins. *Nature* 426, 83–87.

Joiner, A. M., Green, W. W., McIntyre, J. C., Allen, B. L., Schwob, J. E. and Martens, J. R. (2015). Primary cilia on horizontal basal cells regulate regeneration of the olfactory epithelium. *J. Neurosci.* 35, 13761–13772.

Konno, A., Shiba, K., Cai, C. and Inaba, K. (2015). Branchial cilia and sperm flagella recruit distinct axonemal components. *PloS One* 10, e0126005.

Larkins, C. E., Aviles, G. D. G., East, M. P., Kahn, R. A. and Caspary, T. (2011). Arl13b regulates ciliogenesis and the dynamic localization of Shh signaling proteins. *Mol. Biol. Cell* 22, 4694–4703.

Li, Y., Tian, X., Ma, M., Jerman, S., Kong, S., Somlo, S. and Sun, Z. (2016). Deletion of ADP ribosylation factor-like GTPase 13B leads to kidney cysts. *J. Am. Soc. Nephrol.* 27, 3628–3638.

Li, X., Yang, S., Deepak, V., Chinipardaz, Z. and Yang, S. (2021). Identification of cilia in different mouse tissues. *Cells* 10, 1623.

Li, Z. A., Cho, J. H., Woodhams, L. G. and Hughes, J. W. (2022). Fluorescence imaging of beta cell primary cilia. *Front. Endocrinol.* 13, 1004136.

Liu, H., Li, W., Zhang, Y., Zhang, Z., Shang, X., Zhang, L., Zhang, S., Li, Y., Somoza, A. V., Delpi, B., et al. (2017). IFT25, an intraflagellar transporter protein dispensable for ciliogenesis in somatic cells, is essential for sperm flagella formation. *Biol. Reprod.* 96, 993–1006.

Liu, Y.-X., Li, W.-J., Zhang, R.-K., Sun, S.-N. and Fan, Z.-C. (2023). Unraveling the intricate cargo-BBSome coupling mechanism at the ciliary tip. *Proc. Natl. Acad. Sci.* 120, e2218819120.

Lu, H., Toh, M. T., Narasimhan, V., Thamilselvam, S. K., Choksi, S. P. and Roy, S. (2015). A function for the Joubert syndrome protein Arl13b in ciliary membrane extension and ciliary length regulation. *Dev. Biol.* 397, 225–236.

Mariani, L. E., Bijlsma, M. F., Ivanova, A. A., Suciu, S. K., Kahn, R. A. and Caspary, T. (2016). Arl13b regulates Shh signaling from both inside and outside the cilium. *Mol. Biol. Cell* 27, 3780–3790.

Mykytyn, K., Mullins, R. F., Andrews, M., Chiang, A. P., Swiderski, R. E., Yang, B., Braun, T., Casavant, T., Stone, E. M. and Sheffield, V. C. (2004). Bardet–Biedl syndrome type 4 (BBS4)-null mice implicate Bbs4 in flagella formation but not global cilia assembly. *Proc. Natl. Acad. Sci.* 101, 8664–8669.

Nielsen, M. G. and Raff, E. C. (2002). The best of all worlds or the best possible world? Developmental constraint in the evolution of β-tubulin and the sperm tail axoneme. *Evol. Dev.* 4, 303–315.

Nishimura, D. Y., Fath, M., Mullins, R. F., Searby, C., Andrews, M., Davis, R., Andorf, J. L., Mykytyn, K., Swiderski, R. E., Yang, B., et al. (2004). Bbs2-null mice have neurosensory deficits, a defect in social dominance, and retinopathy associated with mislocalization of rhodopsin. *Proc. Natl. Acad. Sci.* 101, 16588–16593.

Nozaki, S., Katoh, Y., Terada, M., Michisaka, S., Funabashi, T., Takahashi, S., Kontani, K. and Nakayama, K. (2017). Regulation of ciliary retrograde protein trafficking by the Joubert syndrome proteins ARL13B and INPP5E. *J. Cell Sci.* 130, 563–576.

Osawa, Y., Murata, K., Usui, M., Kuba, Y., Le, H. T., Mikami, N., Nakagawa, T., Daitoku, Y., Kato, K., Shawki, H. H., et al. (2021). EXOC1 plays an integral role in spermatogonia pseudopod elongation and spermatocyte stable syncytium formation in mice. *eLife* 10, e59759.

Pintado, P., Sampaio, P., Tavares, B., Montenegro-Johnson, T. D., Smith, D. J. and Lopes, S. S. (2017). Dynamics of cilia length in left-right development. *R. Soc. Open Sci.* 4, 161102.

Sakaue-Sawano, A., Kurokawa, H., Morimura, T., Hanyu, A., Hama, H., Osawa, H., Kashiwagi, S., Fukami, K., Miyata, T., Miyoshi, H., et al. (2008). Visualizing spatiotemporal dynamics of multicellular cell-cycle progression. *Cell* 132, 487–498.

San Agustin, J. T., Pazour, G. J. and Witman, G. B. (2015). Intraflagellar transport is essential for mammalian spermiogenesis but is absent in mature sperm. *Mol. Biol. Cell* 26, 4358–4372.

Schindelin, J., Arganda-Carreras, I., Frise, E., Kaynig, V., Longair, M., Pietzsch, T., Preibisch, S., Rueden, C., Saalfeld, S., Schmid, B., et al. (2012). Fiji: an open-source platform for biological-image analysis. *Nat. Methods* 9, 676–682.

Schmitz, F., Burtscher, I., Stauber, M., Gossler, A. and Lickert, H. (2017). A novel Cre-inducible knock-in ARL13B-tRFP fusion cilium reporter. *Genesis* 55, e23073.

Seixas, C., Choi, S. Y., Polgar, N., Umberger, N. L., East, M. P., Zuo, X., Moreiras, H., Ghossoub, R., Benmerah, A., Kahn, R. A., et al. (2016). Arl13b and the exocyst interact synergistically in ciliogenesis. *Mol. Biol. Cell* 27, 308–320.

Shi, L., Zhou, T., Huang, Q., Zhang, S., Li, W., Zhang, L., Hess, R. A., Pazour, G. J. and Zhang, Z. (2019). Intraflagellar transport protein 74 is essential for spermatogenesis and male fertility in mice. *Biol. Reprod.* 101, 188–199.

Su, C.-Y., Bay, S. N., Mariani, L. E., Hillman, M. J. and Caspary, T. (2012). Temporal deletion of *Arl13b* reveals that a mispatterned neural tube corrects cell fate over time. *Development* 139, 4062–4071.

Suciu, S. K., Long, A. B. and Caspary, T. (2021). Smoothened and ARL13B are critical in mouse for superior cerebellar peduncle targeting. *Genetics* 218, iyab084.

Sun, Z., Amsterdam, A., Pazour, G. J., Cole, D. G., Miller, M. S. and Hopkins, N. (2004). A genetic screen in zebrafish identifies cilia genes as a principal cause of cystic kidney. *Development* 131, 4085–4093.

Terry, T. T., Gigante, E. D., Alexandre, C. M., Brewer, K. M., Engle, S. E., Yue, X., Berbari, N. F., Vaisse, C. and Caspary, T. (2023). Ciliary ARL13B prevents obesity in mice.

Thomas, S., Cantagrel, V., Mariani, L., Serre, V., Lee, J.-E., Elkhartoufi, N., De Lonlay, P., Desguerre, I., Munnich, A., Boddaert, N., et al. (2015). Identification of a novel ARL13B variant in a Joubert syndrome-affected patient with retinal impairment and obesity. *Eur. J. Hum. Genet.* 23, 621–627.

Van Sciver, R. E., Long, A. B., Katz, H. G., Gigante, E. D. and Caspary, T. (2023). Ciliary ARL13B inhibits developmental kidney cystogenesis in mouse. *Dev. Biol.* 500, 1–9.

Zhang, Q., Li, Y., Zhang, Y., Torres, V. E., Harris, P. C., Ling, K. and Hu, J. (2016). GTP-binding of ARL-3 is activated by ARL-13 as a GEF and stabilized by UNC-119. *Sci. Rep.* 6, 24534.

Zhang, Y., Liu, H., Li, W., Zhang, Z., Shang, X., Zhang, D., Li, Y., Zhang, S., Liu, J., Hess, R. A., et al. (2017). Intraflagellar transporter protein (IFT27), an IFT25 binding partner, is essential for male fertility and spermiogenesis in mice. *Dev. Biol.* 432, 125–139.

FIGURE LEGENDS

Figure 1. *Arl13b$^{hnn/hnn}$;Arl13b-Cerulean* mice are viable.

A) Percentages of expected (gray) and observed (black) pups from nine litters of *Arl13b$^{hnn/+}$;Arl13b-Cerulean* intercrosses genotyped at 2 weeks. Dashed gray bar indicates *Arl13b$^{hnn/hnn}$* pups predicted by Mendelian ratios; this genotype doesn't survive past embryogenesis. **B)** *Arl13b$^{hnn/+}$;Arl13b-Cerulean* (control) and *Arl13b$^{hnn/hnn}$;Arl13b-Cerulean* (rescue) female mice at 21 weeks. **C)** Weekly body weights of male and female control (black) and *Arl13b$^{hnn/hnn}$;Arl13b-Cerulean* (blue) mice. **D)** Western blot analysis of E12.5 whole-embryo lysates probed with antibody against ARL13B (top blot) and actin loading control (bottom blot).

Figure 2. *Arl13b-Cerulean* rescues *Arl13b$^{hnn/hnn}$* MEF ciliary phenotypes.

Immortalized and serum-starved **A)** *Arl13b$^{+/+}$*, **B)** *Arl13b$^{hnn/hnn}$*, and **C)** *Arl13b$^{hnn/hnn}$;Arl13b-Cerulean* MEFs stained with antibodies against ARL13B, GFP (recognizes Cerulean), and glutamylated tubulin GT335 (cilia marker). **D)** Percent ciliation (cilia/cells) for *Arl13b$^{+/+}$*, *Arl13b$^{hnn/+}$*, and *Arl13b$^{hnn/hnn}$* cells without (0), or with (1, 2 copies) *Arl13b-Cerulean*, as indicated. **E)** Ciliary length based on the GT335 channel. In the graphs, each point represents data from a single field of view with at least 150 total cilia examined for each genotype. One-way ANOVA with Tukey's multiple comparisons test, adjusted *p* values: ns, not significant; **p*<0.05; ****p*<0.001; *****p*<0.0001.

Figure 3. *Arl13b$^{hnn/hnn}$;Arl13b-Cerulean* kidneys do not develop cysts.

Kidney sections from adult **A)** *Arl13b$^{+/+}$*, **B)** *Arl13b$^{hnn/+}$;Arl13b-Cerulean*, and **C)** *Arl13b$^{hnn/hnn}$;Arl13b-Cerulean* mice stained with hematoxylin-eosin or antibodies against ARL13B, GFP, and glutamylated tubulin GT335. **D)** Kidney weight as a percentage of body weight for control (black) and *Arl13b$^{hnn/hnn}$;Arl13b-Cerulean* (blue) male and female mice. Unpaired *t*-test, *p* values: ns, not significant; **p*<0.05. **E)** Morphology of control and rescue kidneys.

Figure 4. Cerebellar patterning is normal in *Arl13b$^{hnn/hnn}$;Arl13b-Cerulean* mice.
A) Sagittal sections of adult control and *Arl13b$^{hnn/hnn}$;Arl13b-Cerulean* cerebella stained with hematoxylin-eosin. Roman numerals indicate major folia. **B)** ARL13B, GFP, and glutamylated tubulin GT335 staining of cilia in the Purkinje cell layer (PCL) of the cerebellum. ML (molecular layer), IGL (inner granule layer). **C)** Choroid plexus of control and *Arl13b$^{hnn/hnn}$;Arl13b-Cerulean* brains stained with ARL13B and GFP antibodies.

Figure 5. *Arl13b$^{hnn/hnn}$;Arl13b-Cerulean* pancreatic islets appear normal.
A) Pancreas sections from control or *Arl13b$^{hnn/hnn}$;Arl13b-Cerulean* mice stained with hematoxylin-eosin. **B)** Immunofluorescent staining of islet cells in control and *Arl13b$^{hnn/hnn}$;Arl13b-Cerulean* pancreas sections using antibodies against glucagon and insulin. **C)** Antibody staining of pancreatic islets showing ciliary ARL13B, GFP, and glutamylated tubulin GT335.

Figure 6. *Arl13b$^{hnn/hnn}$;Arl13b-Cerulean* males are infertile.
A) Average pups born per litter to *Arl13b$^{hnn/+}$;Arl13b-Cerulean* (control) and *Arl13b$^{hnn/hnn}$;Arl13b-Cerulean* (rescue) females mated with control males. Sample *n* = litters counted. **B)** Average pups born per litter to *Arl13b$^{hnn/+}$;Arl13b-Cerulean* (control) and *Arl13b$^{hnn/hnn}$;Arl13b-Cerulean* (rescue) males mated with control females. Sample *n* = litters counted (control) or males tested (rescue). **C)** Testis weight as a percentage of body weight for control and *Arl13b$^{hnn/hnn}$;Arl13b-Cerulean* male mice. For each graph, unpaired *t*-test: ns, not significant, ****$p<0.0001$. **D)** Testis sections from adult *Arl13b$^{+/+}$* and *Arl13b$^{hnn/hnn}$;Arl13b-Cerulean* males stained with PAS-H. **E)** Epididymis sections from adult *Arl13b$^{+/+}$* and *Arl13b$^{hnn/hnn}$;Arl13b-Cerulean* males stained with hematoxylin-eosin. Enlarged images show tubules from cauda epididymis. **F)** Adult testis sections stained with peanut agglutinin lectin (PNA, acrosome) and antibodies against FGFR1OP (FOP, centrosome), acetylated tubulin (AcTub, cilia), and Hoechst (nuclei). Dashed yellow lines indicate the basal lamina of the seminiferous tubule. Lu (lumen). **G)** Immunofluorescence of isolated control and *Arl13b$^{hnn/hnn}$;Arl13b-Cerulean* sperm: stained with PNA, AcTub, and Hoechst. Insets show sperm heads.

Figure 7. ARL13B-Cerulean is expressed in testis and sperm.

A) Immunoblot (IB) of lysates from adult testes probed with antibodies against ARL13B, GFP, and actin. **B)** Adult testis sections from *Arl13b*$^{+/+}$ and *Arl13b*$^{hnn/hnn}$*;Arl13b-Cerulean* males stained with antibodies against ARL13B, GFP, glutamylated tubulin GT335, and Hoechst. Dashed yellow lines indicate basal lamina of the seminiferous tubule. Arrowheads point to cilia. **C)** Sperm isolated from cauda epididymides of *Arl13b*$^{+/+}$, *Arl13b*$^{hnn/+}$*;Arl13b*-Cerulean, and *Arl13b*$^{hnn/hnn}$*;Arl13b-Cerulean* males imaged by phase contrast and fluorescence microscopy using antibodies against glutamylated tubulin GT335, ARL13B, and GFP. Nuclei are stained with Hoechst.

Table S1. Antibodies used in this study

Antibody	Manufacturer	Catalog number	Dilution (purpose)
Polyclonal rabbit anti-ARL13B	ProteinTech	17711-1-AP	1:2000 (IB) 1:1000 (IF)
Polyclonal chicken anti-GFP	Abcam	Ab13970	1:1000 (IF)
Mouse anti-glutamylated tubulin (GT335)	AdipoGen	AG-2032020	1:1000 (IF)
Monoclonal mouse anti-acetylated tubulin (AcTub)	Sigma	T6793	1:2500 (IF)
Polyclonal rabbit anti-insulin	Cell Signaling	3014	1:1000 (IF)
Monoclonal mouse anti-glucagon	Abcam	Ab10988	1:500 (IF)
Polyclonal rabbit anti-FGFR1OP (FOP)	ProteinTech	11343-1-AP	1:500 (IF)
PNA-rhodamine	Vector Labs	RL-1072	1:1000 (IF)
AlexaFluor-conjugated secondary	ThermoFisher	A11039, A31572, A21206, A11029, A21202	1:500 (IF)
Goat anti-mouse-AF647	Jackson Immuno	115-606-003	1:500 (IF)
Polyclonal rabbit anti-GFP	Abcam	Ab290	1:1000 (IB)
Actin-rhodamine	Bio-Rad	12004163	1:5000 (IB)
IR680LT secondary	LI-COR	926-68020	1:5000 (IB)
IR800CW secondary	LI-COR	925-32213	1:5000 (IB)

IF, immunofluorescence; IB, immunoblotting

Figure S1. Complete weight analysis and quantification of embryonic protein expression.

Body weights of control (black) and *Arl13b*$^{hnn/hnn}$*;Arl13b-Cerulean* (blue) **A)** male and **B)** female mice at the time of sacrifice. **C)** Quantification of the signal intensity for western blot shown in Fig. 1D. Data are normalized to actin and set relative to the ARL13B band intensity in wild-type embryos (*Arl13b*$^{+/+}$).

Figure S2. Expression of ARL13B-Cerulean and ARL13B in MEF lines.

A) Percent ARL13B-positive and **B)** GFP-positive cilia for *Arl13b*$^{+/+}$, *Arl13b*$^{hnn/+}$, and *Arl13b*$^{hnn/hnn}$ cells without (0), or with (1, 2 copies) *Arl13b-Cerulean*, as indicated. Each point represents data from a single field of view with at least 150 cilia examined for each genotype. One-way ANOVA with Tukey's multiple comparisons test, adjusted *p* values: ns, not significant; ***$p<0.001$, ****$p<0.0001$. **C)** Immunoblot analysis of MEF lysates probed with antibody against ARL13B. The actin loading control is shown below. **D)** Quantification of the signal intensity for western blot shown in Fig. S2C, with data normalized to actin and set relative to the ARL13B band intensity in wild-type MEFs. **E)** Graphic representation showing locations of primers used in qRT-PCR. **F)** Quantification of transcript levels for endogenous *Arl13b* (black) and *Arl13b-Cerulean* (blue) in cell lines, normalized to *Gapdh* and set relative to *Arl13b* expression in wild-type MEFs.

Figure S3. *Arl13b*$^{hnn/hnn}$*;Arl13b-Cerulean* kidneys do not exhibit fibrosis.

Sirius red-fast green staining of **A)** *Arl13b*$^{+/+}$, **B)** *Arl13b*$^{hnn/+}$*;Arl13b-Cerulean*, and **C)** *Arl13b*$^{hnn/hnn}$*;Arl13b-Cerulean* kidney sections. Reddish-purple color indicates collagen associated with fibrosis, and green shows counterstain. **D-E)** Kidney weight versus body weight of control (black) and *Arl13b*$^{hnn/hnn}$*;Arl13b-Cerulean* (blue) **D)** male and **E)** female mice at time of sacrifice.

Figure S4. Enlarged ventricles in *Arl13b*$^{hnn/hnn}$*;Arl13b-Cerulean* mice.

A) Coronal sections through the lateral ventricles of adult control and *Arl13b*$^{hnn/hnn}$*;Arl13b-Cerulean* brains stained with hematoxylin-eosin. **B)** Western blot showing lysates from cerebella of all mouse genotypes probed with antibodies against

ARL13B and GFP. Actin loading control is shown below. IB, immunoblot. **C)** Quantification of signal intensity for ARL13B western blot shown in Fig. S4B with data normalized to actin and set relative to the ARL13B band intensity in wild-type cerebellum. **D)** Quantification of signal intensity for GFP western blot shown in Fig. S4B with data normalized to actin and set relative to the ARL13B-Cerulean band intensity in *Arl13b+/+;Arl13b-Cerulean* cerebellum (lane 2).

Figure S5. Measurement of fertility parameters.
A) Testis weight versus body weight of control (black) and *Arl13b*$^{hnn/hnn}$*;Arl13b-Cerulean* (blue) males. **B)** Sperm tail length, with at least 65 sperm measured per genotype, including samples from at least three males per genotype. Unpaired *t*-test: ****$p<0.0001$. **C)** Images of sperm under brightfield microscopy, 10x magnification. **D)** Sperm count measured by CASA, $n = 1$ of each genotype. **E)** Sperm motility measured by CASA, $n = 1$ of each genotype.

Figure S6. Expression of ARL13B-Cerulean and ARL13B in testis and epididymis.
A) Quantification of signal intensity for ARL13B western blot shown in Fig. 7A with data normalized to actin and set relative to the ARL13B band intensity in wild-type testis. **B)** Quantification of signal intensity for GFP western blot shown in Fig. 7A with data normalized to actin and set relative to the ARL13B-Cerulean band intensity in *Arl13b+/+;Arl13b-Cerulean* testis (lane 2). **C)** Adult epididymis sections from *Arl13b*$^{+/+}$ and *Arl13b*$^{hnn/hnn}$*;Arl13b-Cerulean* males stained with antibodies against ARL13B, GFP, glutamylated tubulin GT335, and Hoechst. Arrowheads point to cilia.

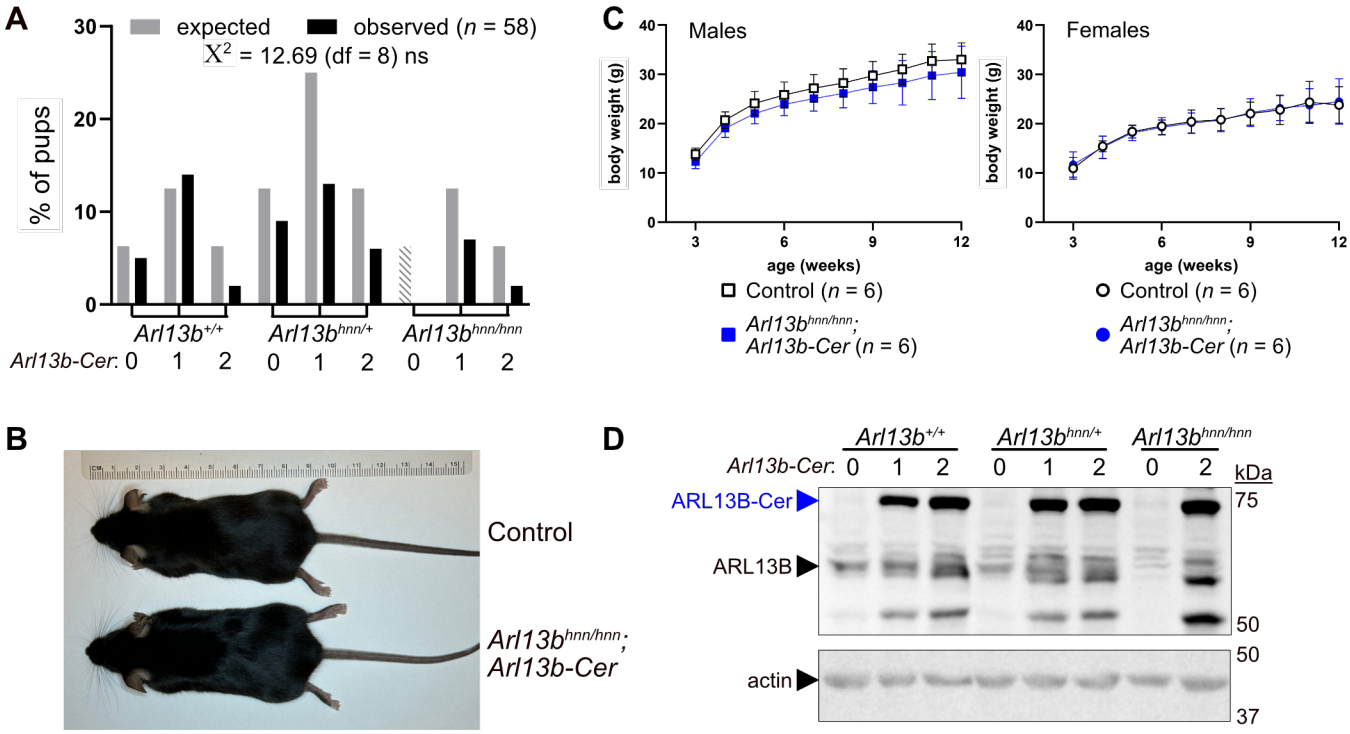
A
expected
observed (n = 58)
X2 = 12.69 (df = 8) ns
% of pups
30
20
10
0
Arl13b+/+
Arl13bhnn/+
Arl13bhnn/hnn
Arl13b-Cer: 0 1 2 0 1 2 0 1 2
C
Males
Females
body weight (g)
age (weeks)
3
6
9
12
Control (n = 6)
Arl13bhnn/hnn; Arl13b-Cer (n = 6)
B
Control
Arl13bhnn/hnn; Arl13b-Cer
D
Arl13b+/+
Arl13bhnn/+
Arl13bhnn/hnn
Arl13b-Cer: 0 1 2 0 1 2 0 2
kDa
ARL13B-Cer
ARL13B
actin
75
50
50
37

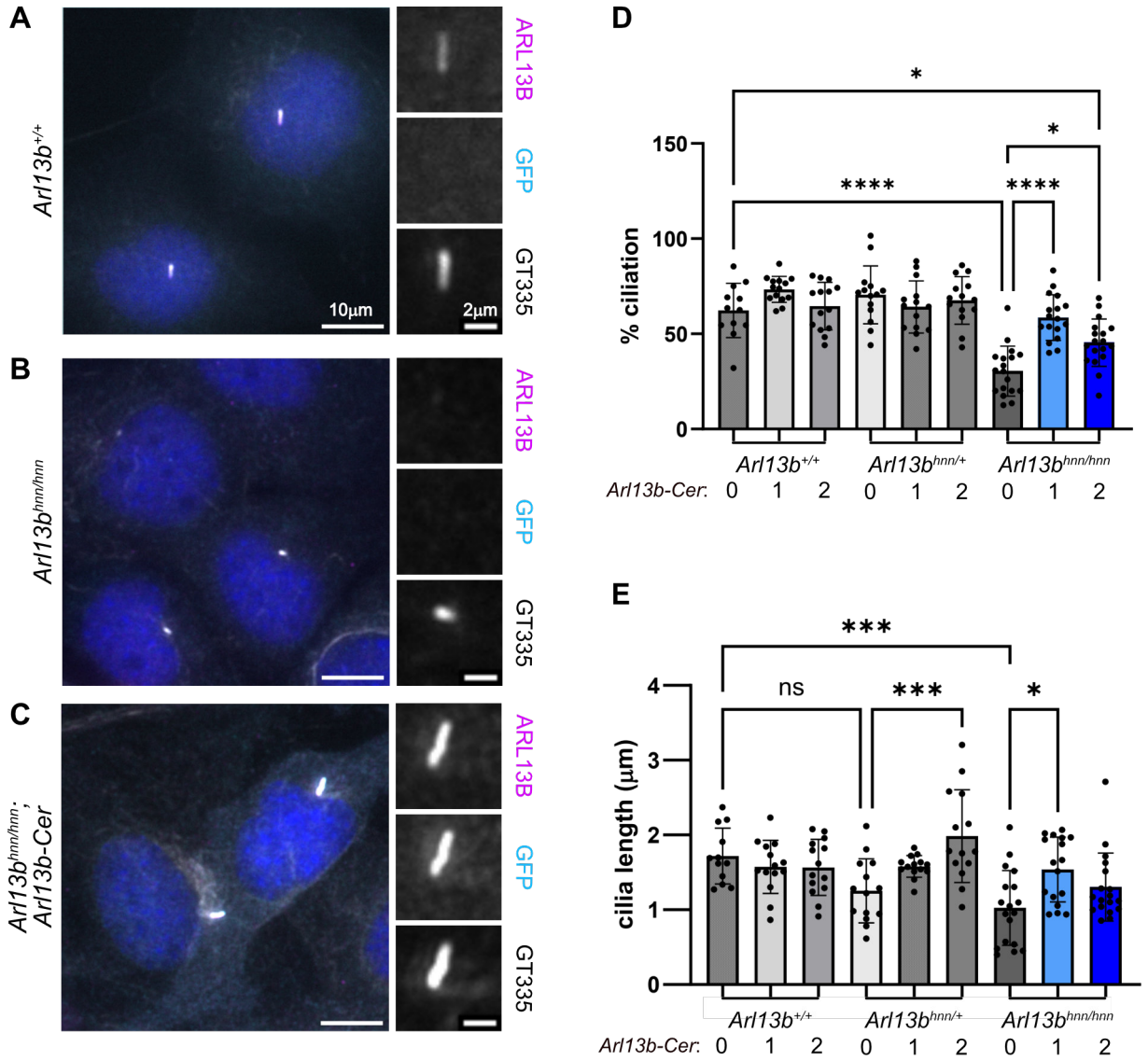
A
Arl13b+/+
10µm
2µm
ARL13B
GFP
GT335
B
Arl13bhnn/hnn
C
Arl13bhnn/hnn; Arl13b-Cer
D
% ciliation
150
100
50
0
*
*
****
****
Arl13b+/+
Arl13bhnn/+
Arl13bhnn/hnn
Arl13b-Cer: 0 1 2 0 1 2 0 1 2
E
cilia length (µm)
4
3
2
1
0
***
ns
***
*
Arl13b+/+
Arl13bhnn/+
Arl13bhnn/hnn
Arl13b-Cer: 0 1 2 0 1 2 0 1 2

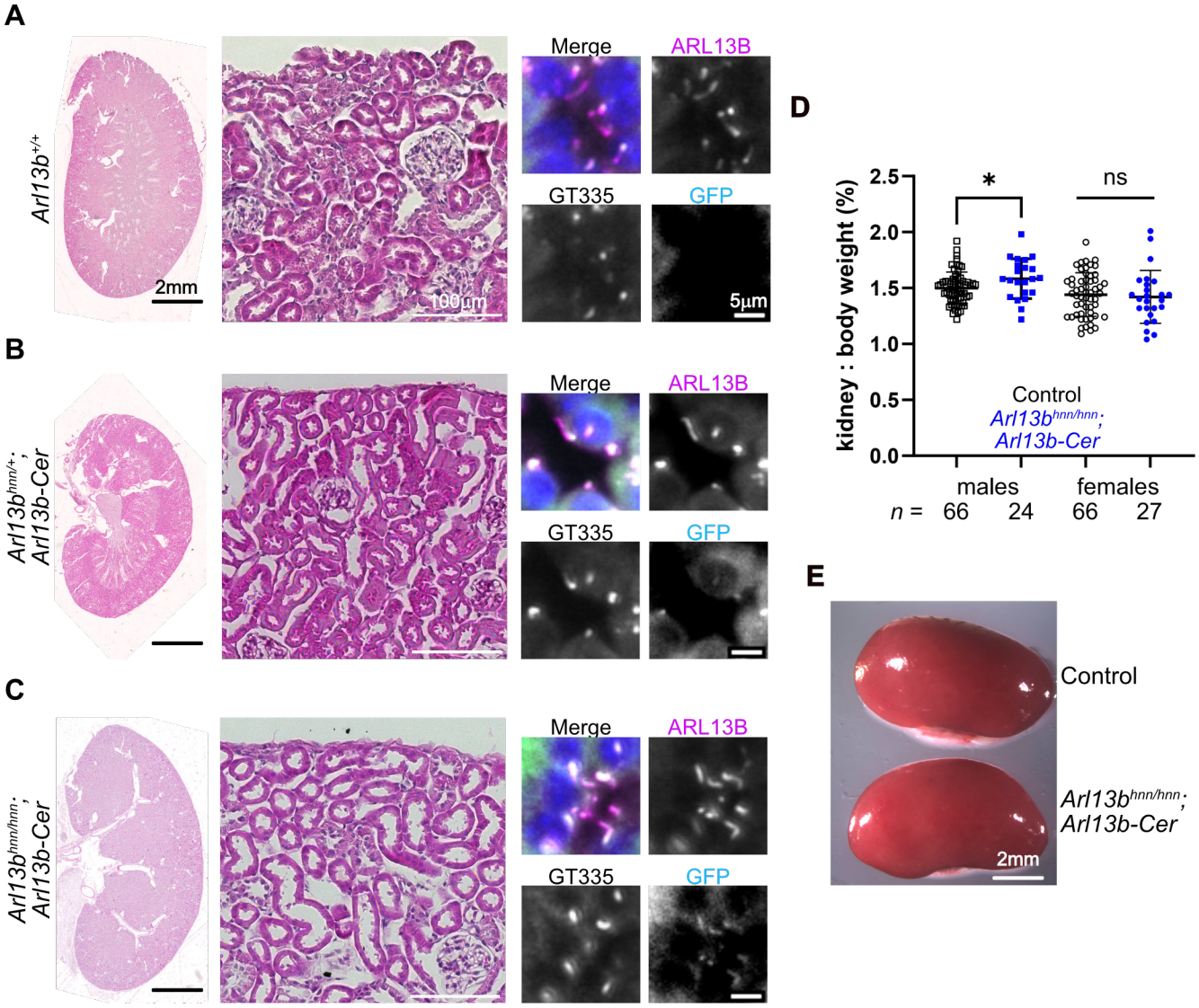
A
Arl13b+/+
2mm
100µm
Merge
ARL13B
GT335
GFP
5µm
B
Arl13bhnn/+; Arl13b-Cer
C
Arl13bhnn/hnn; Arl13b-Cer
D
kidney : body weight (%)
2.5
2.0
1.5
1.0
0.5
0.0
*
ns
Control
Arl13bhnn/hnn; Arl13b-Cer
males
females
n = 66 24 66 27
E
Control
Arl13bhnn/hnn; Arl13b-Cer
2mm

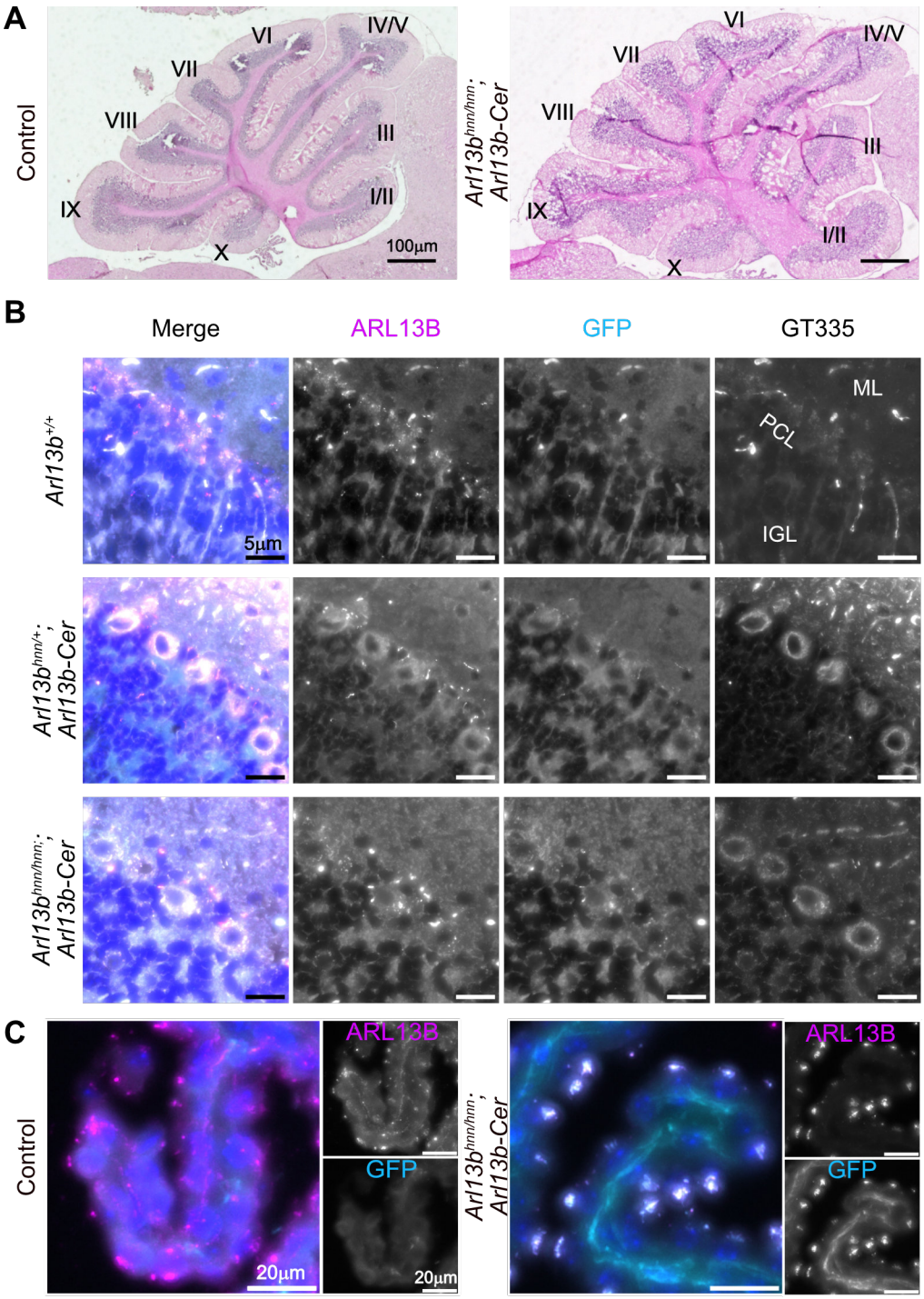
A
Control
VI
IV/V
VII
VIII
III
I/II
IX
X
100µm
Arl13b hnn/hnn ; Arl13b-Cer
B
Merge
ARL13B
GFP
GT335
Arl13b +/+
ML
PCL
IGL
5µm
Arl13b hnn/+ ; Arl13b-Cer
Arl13b hnn/hnn ; Arl13b-Cer
C
Control
ARL13B
GFP
20µm
Arl13b hnn/hnn ; Arl13b-Cer

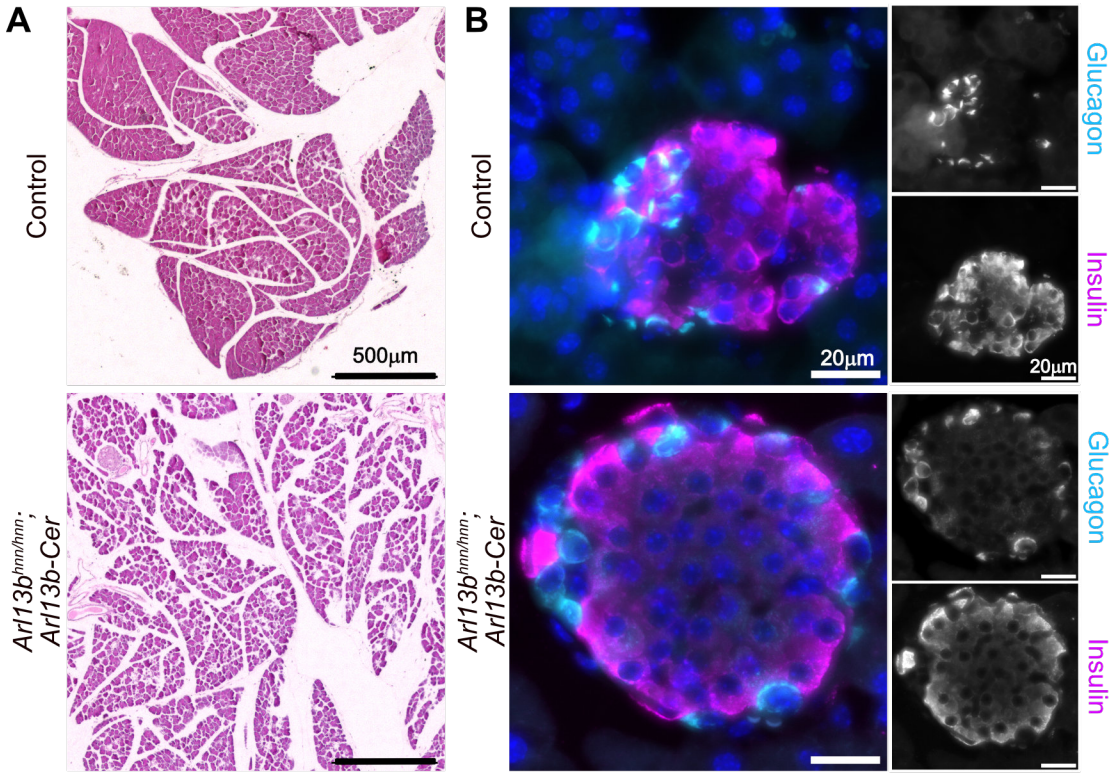
A
Control
500µm
Arl13b^hnn/hnn; Arl13b-Cer
B
Control
20µm
Glucagon
Insulin
20µm
Arl13b^hnn/hnn; Arl13b-Cer
Glucagon
Insulin

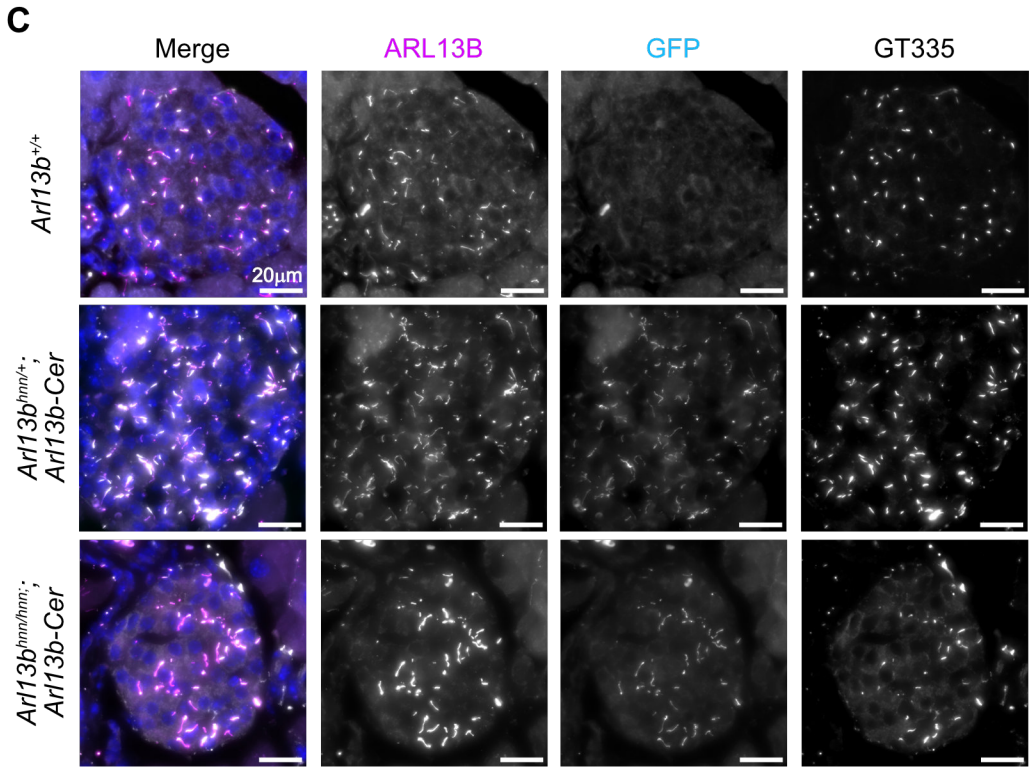
C
Merge
ARL13B
GFP
GT335
Arl13b^+/+
20µm
Arl13b^hnn/+; Arl13b-Cer
Arl13b^hnn/hnn; Arl13b-Cer

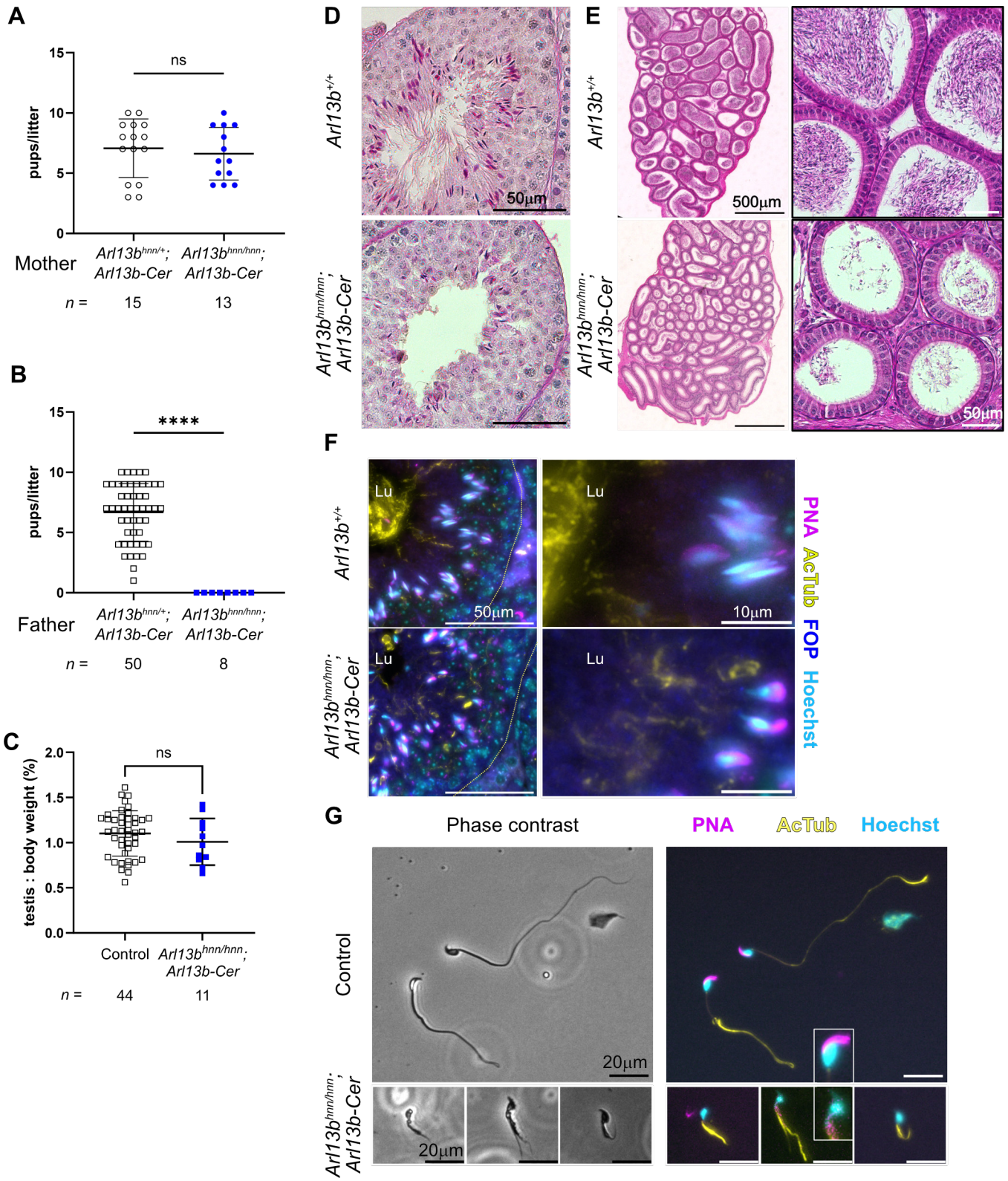
A
ns
pups/litter
15
10
5
0
Mother
Arl13b^hnn/+; Arl13b-Cer
Arl13b^hnn/hnn; Arl13b-Cer
n = 15 13
B
****
pups/litter
Father
n = 50 8
C
ns
testis : body weight (%)
2.0
1.5
1.0
0.5
0.0
Control
Arl13b^hnn/hnn; Arl13b-Cer
n = 44 11
D
Arl13b+/+
Arl13b^hnn/hnn; Arl13b-Cer
50µm
E
500µm
50µm
F
Lu
50µm
10µm
PNA AcTub FOP Hoechst
G
Phase contrast
PNA AcTub Hoechst
Control
20µm

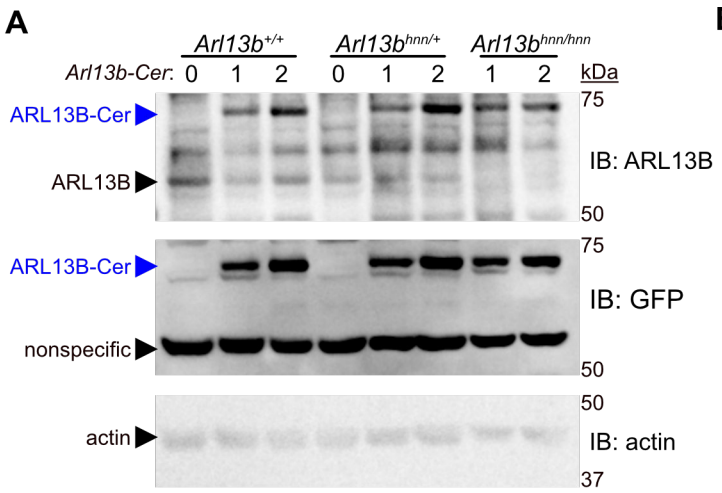
A
Arl13b+/+
Arl13bhnn/+
Arl13bhnn/hnn
Arl13b-Cer: 0 1 2 0 1 2 1 2
kDa
ARL13B-Cer
ARL13B
75
50
IB: ARL13B
ARL13B-Cer
nonspecific
75
50
IB: GFP
actin
50
37
IB: actin

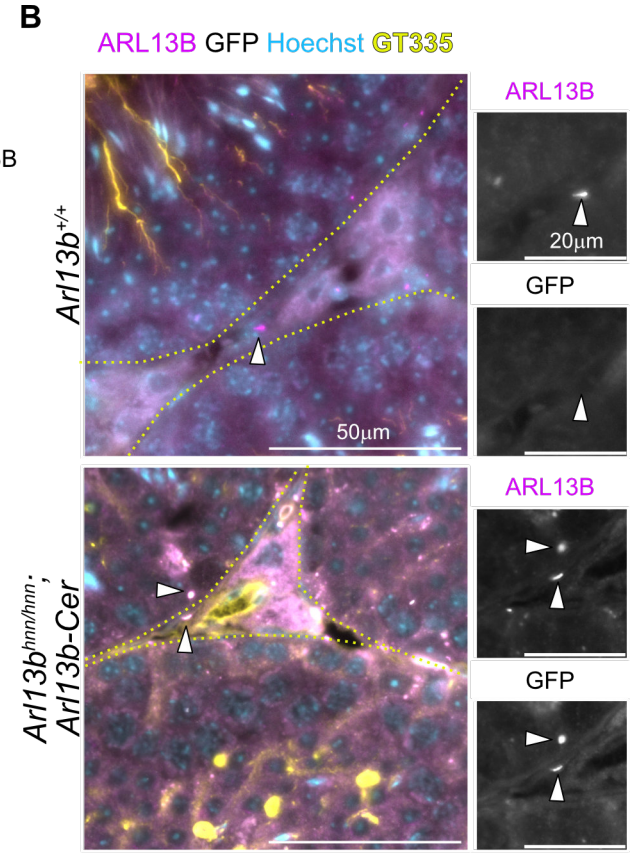
B
ARL13B GFP Hoechst GT335
Arl13b+/+
Arl13bhnn/hnn; Arl13b-Cer
ARL13B
GFP
20μm
50μm

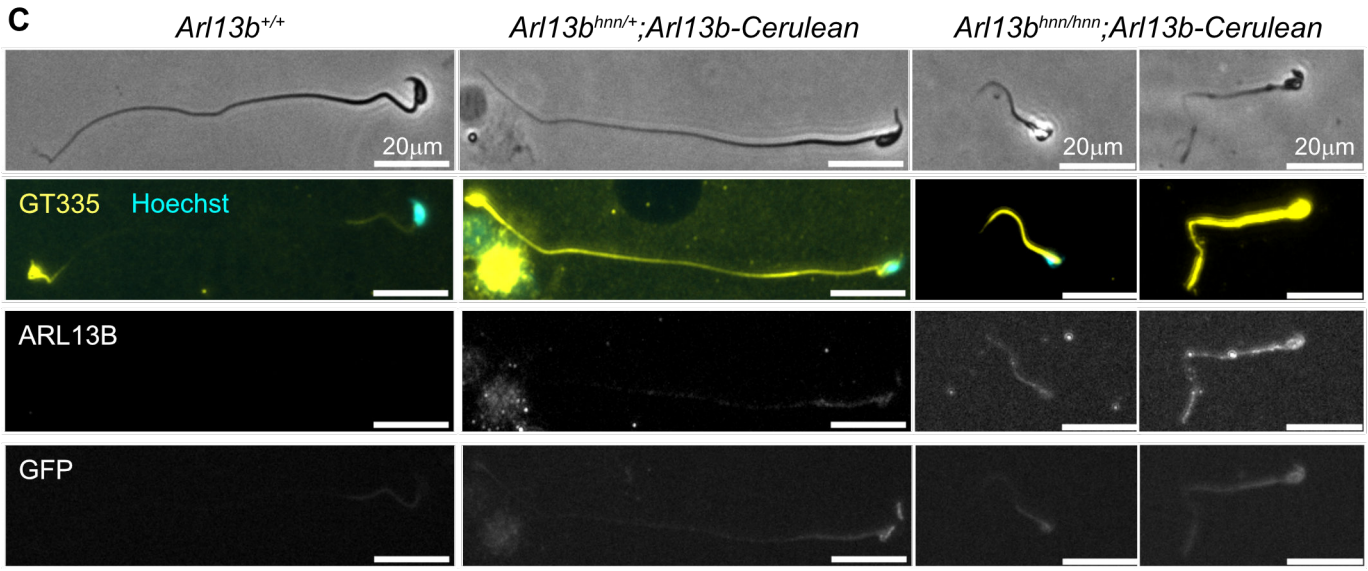
C
Arl13b+/+
Arl13bhnn/+;Arl13b-Cerulean
Arl13bhnn/hnn;Arl13b-Cerulean
20μm
GT335 Hoechst
ARL13B
GFP